Mechanism of the Catalytic Carboxylation of Alkylboronates with CO_2 using Ni-NHC complexes: A DFT Study

Maicon Delarmelina,[a] Enrico Marelli,[b] José Walkimar de M. Carneiro,[a] Steven P. Nolan[c] and Michael Bühl*[b]

Abstract: A new mechanism is proposed for the Ni-catalysed carboxylation of organoboronates with CO_2. DFT investigations at the PBE0-D3 level have shown that direct CO_2 addition to the catalysts [Ni(NHC)(Allyl)Cl] (**1**$_{NHC}$, NHC = IMe, IPr, SIPr and IPr*) is kinetically disfavored and formation of the Aresta-type intermediate is unlikely to occur. According to the mechanism proposed here, the carboxylation process starts with addition of the borate species to **1**$_{NHC}$, followed by transmetalation, CO_2 cycloaddition and carboxylation. The rate-determining step was identified as being the transmetalation process, with computed relative free energy barriers of 34.8, 36.8 and 33.5 kcal mol^{-1} for **1**$_{IPr}$, **1**$_{SIPr}$ and **1**$_{IPr*}$, respectively.

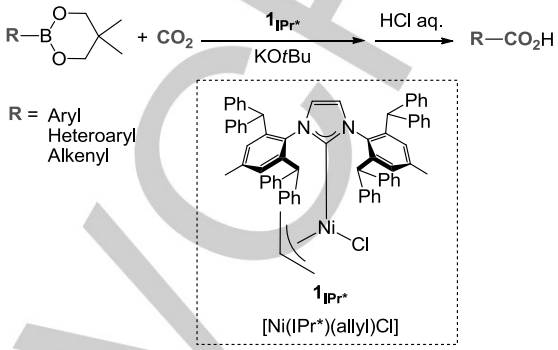

Scheme 1. Nickel-catalyzed carboxylation of boronates.

Introduction

CO_2 is a widely available and inexpensive C1-building block, and its use in organic synthesis is highly attractive, yet challenging. [1,2] The catalytic conversion of CO_2 into useful chemicals, employing both transition metals and organocatalysts, has recently received considerable attention. Pioneering work by Inoue included the direct carboxylation of 1,3-dienes [3] and alkynes [4] using Pd- and Ni-based catalysts, respectively. More recently, Iwasawa reported the first carboxylation of organoboronates in the presence of a rhodium catalyst.[5] Copper- [6,7] and silver-based[8] catalytic systems for this reaction have been developed subsequently, and Nolan recently reported a nickel catalyst for this reaction (see **Scheme 1**). [9] These findings triggered the attention of the synthetic community, leading to intense studies in the field. [10]

Despite the numerous variations in metal-catalyzed protocols for the carboxylation of organoboronate derivatives, the mechanism of such a transformation remains unknown. In particular, for the Ni-promoted version of this reaction, the paramount effect of the IPr* ligand (IPr*: 1,3-bis(2,6-bis(diphenylmethyl)-4-methylphenyl)imidazol-2-ylidene) when compared to smaller ancillary ligands, is a fascinating feature. Also, the requirement of cyclic boronic esters, as opposed to simple boronic acids, is not well understood. Our aim in this report is to understand the reaction mechanism of the Ni-catalyzed carboxylation of organoboronates, while clarifying the role of the flexible steric bulk of the ancillary ligand employed.

[a] Prof. J. W. de M. Carneiro, M. Delarmelina
Universidade Federal Fluminense
Instituto de Química
Niterói, Rio de Janeiro, 24020-141, Brazil
[b] Prof. M. Bühl, E. Marelli
University of St Andrews
School of Chemistry
North Haugh, St Andrews, Fife, KY16 9ST, Scotland (UK)
E-mail: buehl@st-andrews.ac.uk
[c] Prof. Dr. S. P. Nolan, Department of Inorganic and Physical Chemistry, Ghent University, Krijgslaan 281 - S3, 9000 Gent, Belgium

Supporting information for this article is given via a link at the end of the document.

Results and Discussion

We investigated four distinct pathways for the Ni-catalyzed carboxylation of organoboronates. In the first hypothesis (**Mechanism A**, **Figure 1**), the Aresta-type intermediate **5**$_{NHC}$ [11] is proposed to be formed after *in situ* generation of the Ni^0 intermediate **4**$_{NHC}$ and subsequent cycloaddition of CO_2 to **4**$_{NHC}$. Alternatively, formation of **5**$_{NHC}$ was also considered to occur by direct CO_2 addition to catalyst **1**$_{NHC}$ with concerted formation of η^2-3-chloro-allyl moiety (**Mechanism B**, **Figure 1**). The third considered pathway (**Mechanism C**, **Figure 1**) begins with the cycloaddition of CO_2 to **1**$_{NHC}$ and simultaneous rearrangement of the allyl moiety from the η^3- to η^1-form.

Finally, the last pathway (**Mechanism D**, **Figure 1**) starts with addition of the borate species to the catalyst **1**$_{NHC}$ and formation of the intermediate **11**$_{NHC}$. Based on the initial mechanistic investigation performed by Nolan *et al*, [9] the borate **3**$_{OR}$ was considered to be the reactive species in the catalytic cycle, rather than the boronate **2**.

Initially, isomer searches for each intermediate and transition state were performed using the simplest phenyl boronate used experimentally, together with smaller congeners of the experimental ligands (**IMe**, **Figure 2**) and base (methoxide anion, **MeO**$^-$). A large number of regioisomers and conformers were considered in each case (see Supporting Information, SI). After identification of the most stable isomers of each intermediate and transition state, they were reoptimised using the experimental ligand **IPr** (**Figure 2**) and *tert*-butoxide (**tBuO**$^-$). The most important points in the catalytic cycle were also reoptimised using the experimental ligands **SIPr** and **IPr*** (**Figure 2**) and were then used for comparison of theoretical efficiency of the catalysts. **1**$_{IPr}$, **1**$_{SIPr}$ and **1**$_{IPr*}$ were chosen due to their distinguished experimental activity, ranging from low (**1**$_{IPr}$) and intermediate (**1**$_{SIPr}$) to high efficiency (**1**$_{IPr*}$). Detailed discussion on each alternative catalytic cycle follows.

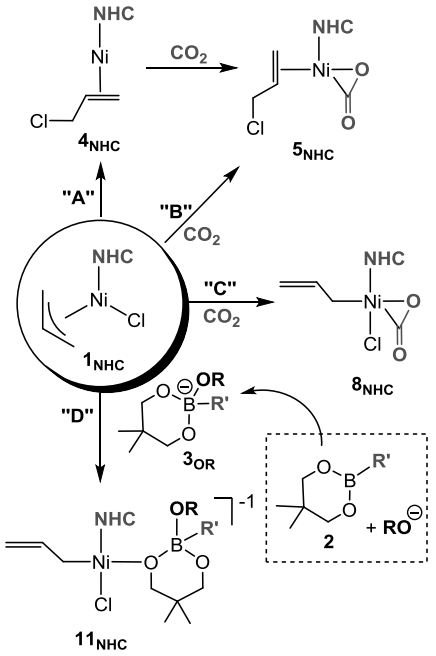

Figure 1. Initial steps for the possible catalytic cycles **A**, **B**, **C** and **D** (R' = aryl; in this study R' = Ph).

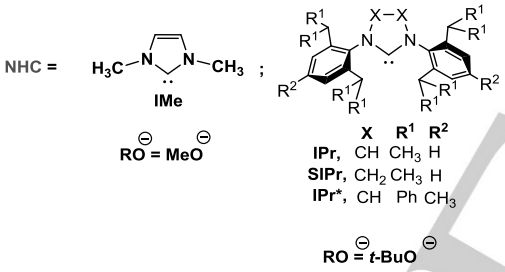

Figure 2. Experimental ligands **IPr, SIPr and IPr***, experimental base *tert*-buthoxy anion (**tBuO**$^-$) and the smaller congeners of the ligands, **IMe**, and base, methoxide anion (**MeO**$^-$).

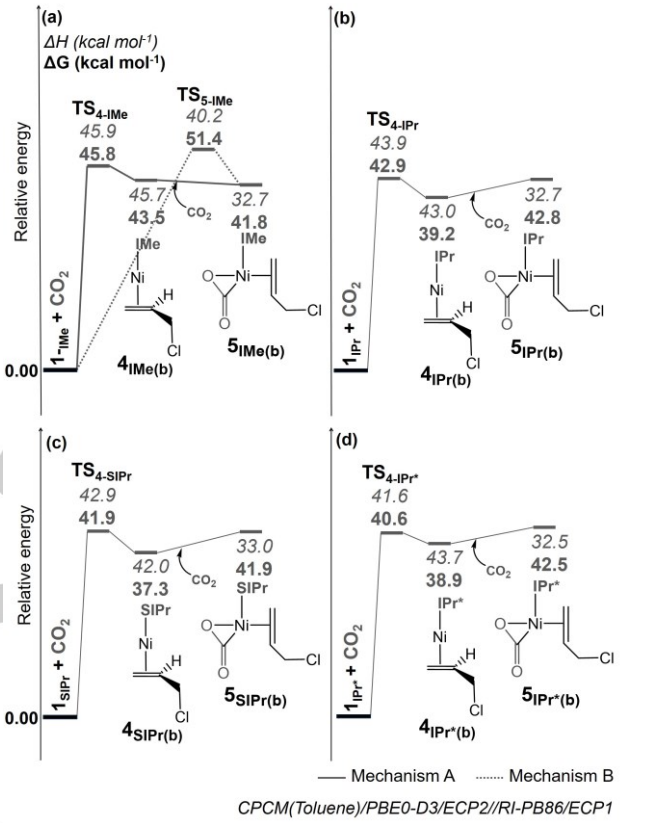

Figure 3. Energy profile for formation of Aresta-type intermediate **5**$_{NHC}$ via **Mechanisms A** and **B**.

coordination site through reformation of allyl chloride is much too unfavourable. This result is consistent with experiment, where the catalysts are prepared from Ni(0) precursors and allyl chloride, without apparent evidence for reversibility. However, the accessibility of such intermediates under the relatively harsh conditions of catalysis could not have been ruled out beforehand.

Formation of an Aresta-type intermediate

Two alternative mechanisms were considered for formation of Aresta-type intermediate **5**$_{IMe}$: mechanisms **A** and **B** (**Figure 1**), which involve reductive elimination of allyl and chloride ligands to afford a η^2-bound allyl chloride. Pre-activation of **1**$_{IMe}$, the first step in mechanism **A**, was computed as highly endergonic (**Figure 3a**), presenting a free-energy barrier of 45.8 kcal mol^{-1}. The relative free energy of the formed intermediate **4**$_{IMe(b)}$ is 43.5 kcal mol^{-1}. Interestingly, no energy barrier was computed for the cycloaddition of CO_2 to **4**$_{IMe(b)}$ to form the intermediate **5**$_{IMe(b)}$.

Considering the second pathway, formation of **5**$_{IMe}$ via **TS**$_{5\text{-}IMe}$ (Mechanism **B**, **Figure 3a**) presented a free-energy barrier 5.6 kcal mol^{-1} higher than mechanism **A** (via **TS**$_{4\text{-}IMe}$, **Figure 3a**). The stationary points **TS**$_{4\text{-}NHC}$, **4**$_{NHC}$ and **5**$_{NHC}$ are slightly stabilised when using the experimental ligands **IPr**, **SIPr** and **IPr*** (**Figures 3b-d**). In these cases, the energy demand for formation of **5**$_{NHC}$ via **TS**$_{4\text{-}NHC}$ decreased by 3-5 kcal mol^{-1}. However, very high, essentially unsurmountable barriers are obtained in each case. Apparently the creation of a vacant

CO_2 cycloaddition to Ni(II)

In the third alternative pathway (Mechanism **C**), differently from the mechanisms presented above, no reductive elimination of allyl chloride is assumed. Instead, $\eta^3 \rightarrow \eta^1$ slippage of the allyl ligand was invoked to create the coordination site for adding CO_2, affording intermediate **8**$_{IMe}$ (**Figure 4**). The free-energy barrier for this concerted process was lower than for formation of Aresta-type intermediate (**5**$_{IMe}$) via mechanism **A** (**Figure 3a**) by 12.2 kcal mol^{-1}.

Although the lower energy barrier for the first step showed mechanism **C** to be possibly favoured, intermediate **8**$_{IMe}$ is unable to proceed through the next step of the catalytic cycle, transmetalation of the phenyl group. Dissociation of the CO_2 molecule was always observed when borate **3**$_{OMe}$ and intermediate **8**$_{IMe}$ were artificially forced to interact. Furthermore, intermediate **9**$_{IMe}$ presented high relative energy and the transition state for this step can be expected to be higher than 40 kcal mol^{-1}, also resulting in a prohibitive step for the cycle.

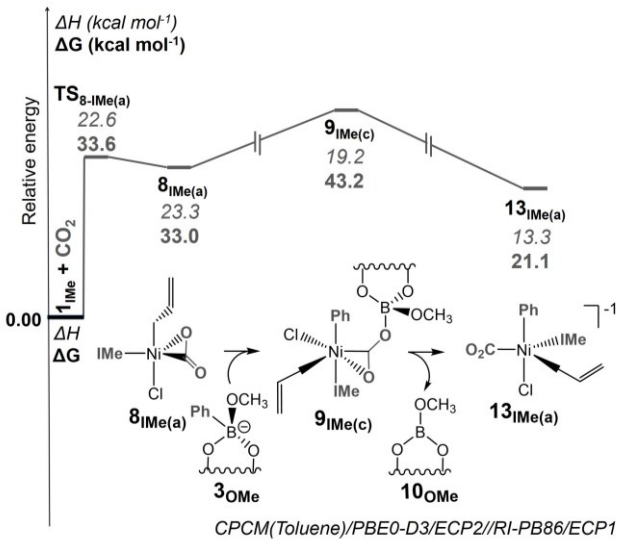

Figure 4. Energy profile for CO_2 cycloaddition to the catalyst **1$_{IMe}$** (Step 1, mechanism **C)**.

Inspired by the high stability of NHC-CO_2 zwitterionic complexes in metal-free conditions,[12] an additional alternative pathway for transmetalation was investigated, considering insertion of CO_2 into the Ni-NHC bond (**Figure S1**). This process, however, was also shown to have high energy barriers (43.2 and 49.2 kcal mol^{-1}, respectively) and was considered unlikely to occur.

Addition of borate to Ni(II)

The final alternative pathway (Mechanism **D**) starts with addition of the borate species to the catalyst **1$_{IMe}$**, accompanied by a concerted reorganization of the allyl moiety from η^3- to η^1-form and formation of the intermediate **11$_{IMe}$** (**Figure 1**). Since any of the oxygen atoms in **3$_{OMe}$** can perform such nucleophilic attack, the most stable isomers of **11$_{IMe}$** were identified (**Figure S5**, Supporting information) and used for preparation of four possible transition structures for this process (**TS$_{11\text{-}IMe(d)}$**, **TS$_{11\text{-}IMe(e)}$**, **TS$_{11\text{-}IMe(h)}$** and **TS$_{11\text{-}IMe(k)}$**, **Figure S14**, Supporting information). The lowest free-energy barrier was obtained with **TS$_{11\text{-}IMe(d)}$**, 14.5 kcal mol^{-1} (**Figure 5(a)**). Compared to the first steps in the previous cycles (**Mechanism A**, **B** and **C**), formation of **11$_{IMe}$** is strongly favoured kinetically as the first intermediate in the reaction mixture.

Due to the conformational complexity of **11$_{IMe}$**, a total of four pathways (**Figure 6**) were considered for transmetalation, the next step in this cycle. Direct transmetalation of **11$_{IMe}$** to **12$_{IMe}$** was the first possibility considered. Alternatively, three additional pathways were evaluated considering dissociation of the chloride ligand, resulting in the formation of intermediates **14$_{IMe}$**, **14'$_{IMe}$** and **14''$_{IMe}$** (**Figure 6**).

Intermediate **14$_{IMe}$** (**Figure 6**) can be formed from **11$_{IMe}$** after migration of the allyl group from η^1- to η^3-form and elimination of the chloride. In a similar way, intermediates **14'$_{IMe}$** and **14''$_{IMe}$** are obtained when the phenyl ring or one of the oxygen atoms in the borate group, respectively, occupies the free coordination site of the metal, previously occupied by the chloride.

The transmetalation product **15$_{IMe}$** can be directly obtained from **14$_{IMe}$** via **TS$_{15\text{-}IMe}$** (**Figure 6**). For transmetalation of **14'$_{IMe}$**, the Ph-B bond is broken and the reactive intermediate **15'$_{IMe}$** is obtained, which can undergo an additional decomposition step with low energy barrier (~5 kcal mol^{-1}, relative to **15'$_{IMe}$**) to afford the transmetalation products **15$_{IMe}$** and **10$_{OMe}$**.

In **14''$_{IMe}$** (**Figure 6**), both oxygen atoms are coordinated to the metal and the phenyl group can been transferred "over" or "under" the coordination plane. However, after initial evaluation of the PES by scan calculations, it was observed that **TS$_{15''\text{-}IMe}$** does not appear to exist. When the phenyl group was artificially transferred over the coordination plane in **14''$_{IMe}$**, one of the oxygen atoms in the borate group was dislocated and the phenyl ring occupied that coordination site. The resulting transition state was the same as in **TS$_{15'\text{-}IMe}$**.

Overall, three possible transition states were identified for the transmetalation step (**TS$_{12\text{-}IMe}$**, **TS$_{15\text{-}IMe}$** and **TS$_{15'\text{-}IMe}$**), which were connected by the chloride association/dissociation equilibrium for **11$_{IMe}$** and **14$_{IMe}$**, or **11$_{IMe}$** and **14'$_{IMe}$**. After thorough isomer search for these three possible transition structures (**Figure S15**, **S17** and **S21**, Supporting information), the most stable species were **TS$_{12\text{-}IMe(e)}$**, **TS$_{15\text{-}IMe(c)}$** and **TS$_{15'\text{-}IMe(n)}$**, with computed free-energy barriers of 39.5, 30.4 and 28.6 kcal mol^{-1} (**Figure 5**), respectively.

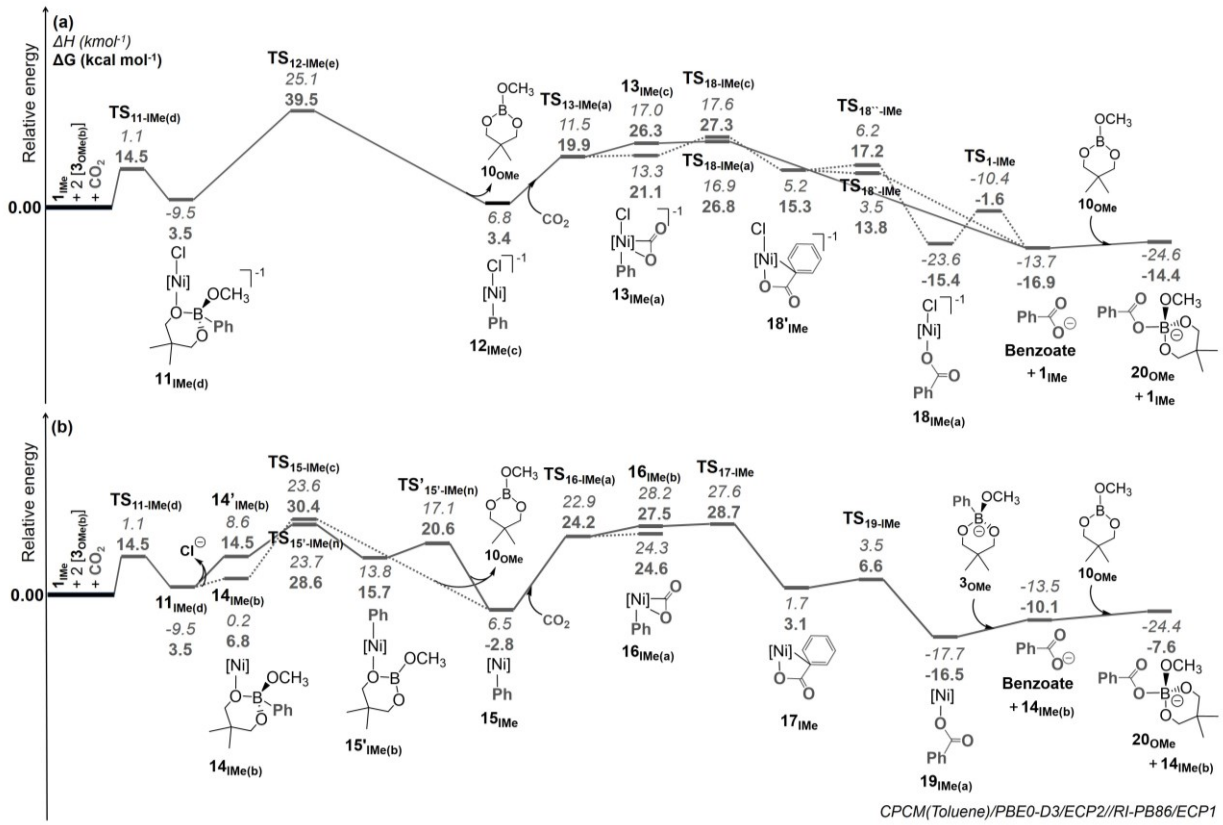

Figure 5. Energy profile for carboxylation of methoxyl phenyl borate (**3$_{OCH3}$**) with CO_2 catalysed by **1$_{IMe}$** via **Mechanism D**.

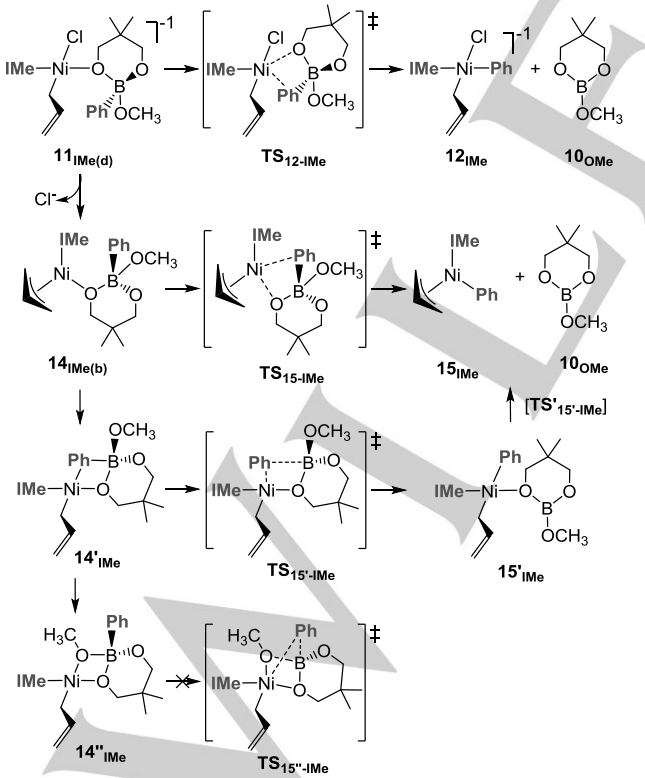

Figure 6. Alternative pathways for phenyl transference process (Step 2, **Mechanism D**) from **11$_{IMe(d)}$**.

Considering the equilibrium between **11$_{IMe}$** and **14$_{IMe}$**, two energy profile (with and without the chloride coordinated, respectively) can be expected for **Mechanism D**. It is worth noting, however, that both profiles are connected, not only by **11$_{IMe}$** and **14$_{IMe}$**, but also by the other intermediates formed in each step (**12$_{IMe}$** and **15$_{IMe}$**; **13$_{IMe}$** and **16$_{IMe}$**; or **18$_{IMe}$** and **19$_{IMe}$**, **Figure 7**), as well as for the experimental catalysts (**Table S1**, Supporting information). The existence of such equilibria can allow each step to occur on a different pathway (**D(a)** or **D(b), Figure 5**), depending on where the lower energy barriers are located. It should be noted that accurate prediction of equilibrium involving small charged species such as free chloride anion is a daunting task for the simple implicit solvation models used here. When including explicit solvation effects of the chloride, the association/dissociation equilibrium presented lower ΔG than when only implicit solvation was considered (**Figure S2**, Supporting information). However, for a more quantitative appraisal, more solvent molecules would have to be included and a more involved (i.e. dynamic) sampling of solute-solvent structures would be necessary.

Both profiles (**D(a)** or **D(b), Figure 5**) consisted of the same initial step (addition of borate to the catalyst, via **TS$_{11\text{-}IMe(d)}$**), with low energy barrier for formation of **11$_{IMe(d)}$**. The second step (transmetalation, via **TS$_{12\text{-}IMe(e)}$**, **TS$_{15\text{-}IMe(c)}$** or **TS$_{15'\text{-}IMe(n)}$**) presented the highest energy barrier in both cycles. In fact, the profile **D(b)** (**Figure 5**) presented the lowest energy pathway for this step, via **TS$_{15'\text{-}IMe(n)}$**, affording **15$_{IMe}$** after decomposition of **15'$_{IMe}$**.

After formation of intermediate **15$_{IMe}$**, the energy of the system increases with CO_2 cycloaddition (third step) via **TS$_{13}$**-

$_{IMe(a)}$ and $TS_{16\text{-}IMe(a)}$ and formation of $13_{IMe(a)}$ and $16_{IMe(a)}$, peaking at the transition states for carboxylation ($TS_{18\text{-}IMe(a)}$ and $TS_{17\text{-}IMe}$), with values for relative free-energy of 26.8 and 28.7 kcal mol^{-1}, respectively. In some cases, transition states that were located on the RI-BP86/ECP1 potential energy surface are lower in enthalpy than the products they connect to at the PBE0-D3/ECP2 level (e.g. 13_{IMe} vs. $TS_{13\text{-}IMe}$); this indicates that the corresponding stationary points do not exist at the higher level (they are an artifact of the lower level employed for optimization) and that the preceding minima connect directly to the subsequent transition states (e.g. $12_{IMe} \rightarrow TS_{15\text{-}IMe}$).

All isomers of 13_{IMe} and 16_{IMe} (**Figure S8** and **S11**, Supporting information) have CO_2 coordinated to the metal at equatorial position. On the other hand, the phenyl group could assume either axial or equatorial position. The lowest transition states for the carboxylation step ($TS_{18\text{-}IMe(a)}$, $TS_{18\text{-}IMe(c)}$ or $TS_{17\text{-}IMe}$, **Figure 5**) were obtained when the phenyl group assumed the axial position (as in isomers $13_{IMe(c)}$, $13_{IMe(a)}$ and $16_{IMe(b)}$, **Figure S8** and **S11**, Supporting information). Such isomers presented the best structural arrangement for the C-C bond forming step between CO_2 and the phenyl group.

Full optimization of $TS_{18\text{-}IMe(c)}$ or $TS_{17\text{-}IMe}$ toward the products gave the reactive intermediates $18'_{IMe}$ and 17_{IMe} (**Figure 5**), which could afford the carboxylated products $18_{IMe(a)}$ and $19_{IMe(a)}$ with low energy barriers. For $TS_{18\text{-}IMe(a)}$ full optimisation led to direct formation of the free benzoate molecule and regeneration of the catalyst 1_{IMe}. Formation of 20_{OMe} was proposed to occur since no solid was observed in the reaction mixture. [9] The free benzoate, associated with the K^+ counterion, would be expected to precipitate in toluene. It is worth noting that for mechanism **D(b)**, intermediate $14_{IMe(d)}$ is restored at the end of the cycle, instead of the initial catalyst 1_{IMe}.

After merging the profiles **D(a)** and **D(b),** selecting the lowest energy pathway for each step and moving to IPr, the following steps were identified as the lowest energetic pathway for the carboxylation process catalyzed by 1_{IPr} (**Figure 8**):

Step 1. Addition of the borate to the catalyst:
($1_{IPr} + 3_{OtBu(b)} \rightarrow 11_{IPr(d)}$)
Step 2. Equilibrium between $11_{IPr(d)}$ and $14'_{IPr(b)}$, with chloride elimination
Step 3. Transmetalation of $14'_{IPr(b)}$ via $TS_{15'\text{-}IPr(h)}$
Step 4. Decomposition of $15'_{IPr}$ into 15_{IPr} and 10_{OtBu}
Step 5. CO_2 Addition via $TS_{13\text{-}IPr(h)}$ or $TS_{16\text{-}IPr(a)}$
Step 6. Carboxylation step via $TS_{17\text{-}IPr}$ or $TS_{18\text{-}IPr(a)}$

Both intermediates $12_{IPr(c)}$ and 15_{IPr} are connected by the equilibrium of the chloride and it is possible that these two transition states for CO_2 cycloaddition ($TS_{13\text{-}IPr(h)}$ and $TS_{16\text{-}IPr(a)}$) may occur under the experimental conditions. The same can be expected for the intermediate $13_{IPr(c)}$ and $16_{IPr(a)}$ and the respective transition states for the carboxylation step, $TS_{18\text{-}IPr(a)}$ and $TS_{17\text{-}IPr}$. The small energy difference between relevant stationary points for both **D(a)** and **D(b)** pathways, considering either enthalpy or free-energy values, does not allow for a clear conclusion onwhich pathway would be favored.

Additionally, full optimisation of intermediate $14'_{IPr}$ (**Figure 8**) resulted in a vacant coordination site, previously occupied by the chloride, as the bulkier ligand prevented the rearrangement of the allyl moiety from η^1- to η^3-form. On the other hand, due to the steric effects of the bulkier ligand, the rearrangement of the allyl moiety from η^1- to η^3-form and nickel-phenyl bond breaking in 17_{IPr} were facilitated and the energy barrier for formation of 19_{IPr} decreased when compared to 17_{IMe} (**Figure 5(b)**).

For the comparison between catalysts, the most important stationary points on the PES for the description of the theoretical efficiency of the catalysts were computed using the ligands **SIPr** and **IPr*** (**Figure S3**, Supporting information). Due to the presence of bulkier ligands, possible changes in the relative stability for some of the isomers might be observed. The best angle between the coordination plane and the imidazole ring of the NHC ligand was also analysed.

According to the Energy Span Model proposed by Kozuch and Shaik, [13] the energy span (δE) of the theoretical cycle **D** for 1_{IPr}, 1_{SIPr} and 1_{IPr*} was calculated using Equation 1 below.

$$\delta E = \Delta E(TDTS - TDI) + \Delta E_{Reaction} \quad (1)$$

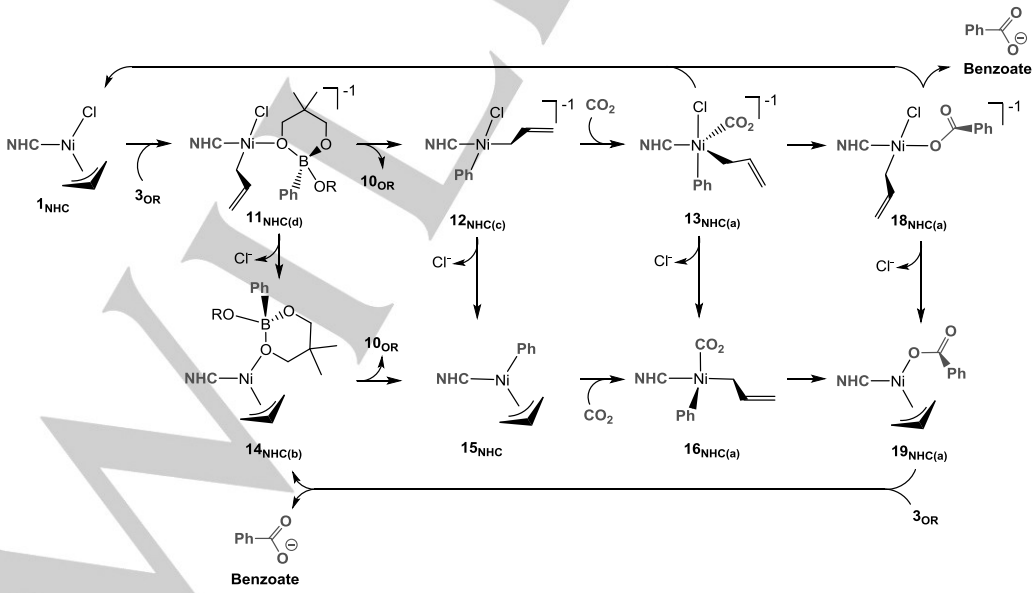

Figure 7. Schematic representation of the key steps in **Mechanism D**, including the alternative pathway via chloride dissociation.

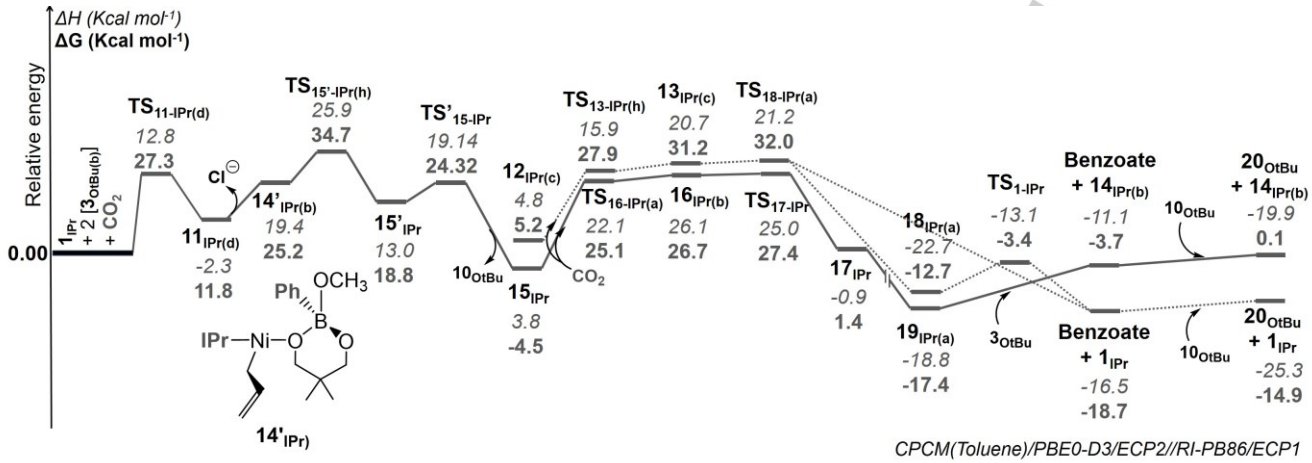

Figure 8. Energy profile for carboxylation of *tert*-buthoxyl phenyl borate (**3**$_{OtBu}$) with CO_2 catalysed by **1**$_{IPr}$ via **Mechanism D**

TDTS and TDI stands for the relative energy of the TOF(Turnover frequency)-Determining Transition State and TOF-Determining Intermediate, respectively. For all catalysts, the TOF-Determining Transition State (TDTS) in mechanism **D** was identified as being **TS**$_{15'\text{-}NHC}$. The TOF-Determining Intermediate (TDI), however, can vary depending on the choice of the NHC ligand or whether the energy span is calculated using enthalpy or Gibbs free energy values. For both **1**$_{IPr}$ and **1**$_{SIPr}$, the lowest points in the cycle are the final products (**1**$_{NHC}$ + Benzoate or **1**$_{NHC}$ + **20**$_{OR}$). For **1**$_{IPr*}$, however, the TDI was identified as being **18**$_{NHC}$ or **19**$_{NHC}$.

The transition structures **TS**$_{12\text{-}NHC}$, **TS**$_{15\text{-}NHC}$ and **TS**$_{15'\text{-}NHC}$ were reoptimised using the experimental ligands **SIPr, IPr*** and **IPr** (**Figure S16**, **S18**-**S20**, **S22**-**S24**, Supporting information). The most stable **TS** was selected to represent the transmetalation step. As observed for **IMe**, **TS**$_{15'\text{-}NHC}$ (NHC = **IPr**, **SIPr** and **IPr***) was obtained as the lowest transition state for transmetalation. For the bulkier ligands, however, **TS**$_{15'\text{-}NHC(h)}$ (NHC = **IPr**, **SIPr** and **IPr***) was identified as the most stable one, rather than **TS**$_{15'\text{-}NHC(n)}$, as observed for **IMe**.

The effect of dispersion is highly significant for the two initial steps of these cycles, in which the boron species is still bound. As the TOF-Determining Transition State **TS**$_{15'\text{-}NHC}$ was present in one of these steps, the points used in the calculation of the energy span were reoptimised including dispersion correction in the optimisation process, The relative energies of the relevant stationary points are shown in **Figure 9**, as well as the calculated energy span (δE) for each ligand.

Despite the noticeably different experimental efficiency of the catalysts **1**$_{IPr}$, **1**$_{SIPr}$ and **1**$_{IPr*}$, the computed energy span presented similar values, ranging from 26.0 to 27.2 kcal mol^{-1} and from 39.0 to 41.0 kcal mol^{-1} for enthalpy and free energy, respectively. These relative high energy barriers are consistent with the high temperatures required for the carboxylation to proceed under the experimental conditions. [9] Note also that the high entropic penalties (i.e. the increase in ΔG over ΔH) arising from associative transition states is likely to be overestimated with our methodology (this problem is well-known, and various workarounds had been proposed, from empirical scaling of entropies[14] to evaluating translational entropies at high pressure to model a condensed phase.[15] However, none of these procedures would change the relative sequence of the barriers across different ligands).

The relative energies of the transition structure **TS**$_{15\text{-}IPr*}$ is lower than **TS**$_{15\text{-}IPr}$ or **TS**$_{15\text{-}SIPr}$ by 1.3-3.3 kcal mol^{-1}, such as it would be expected for the bulkier system due to the additional stabilization provided by the ligand **IPr*** (**Figure 9**). The same effect was observed for intermediates **18**$_{IPr*}$ and **19**$_{IPr*}$, which presented lower relative energies than the congener containing **IPr** and **SIPr**. The decrease of the relative energy of **TS**$_{15\text{-}IPr*}$ (by 1.3 and 3.3 kcal mol^{-1} when compared to **TS**$_{15\text{-}IPr}$ or **TS**$_{15\text{-}SIPr}$), however, is much smaller than those of **18**$_{IPr*}$ and **19**$_{IPr*}$. As a result, the calculated energy span for **1**$_{IPr*}$ was similar to that of the catalysts which presented higher relative energies for the TOF-determining transition state (**TS**$_{15\text{-}IPr}$ or **TS**$_{15\text{-}SIPr}$).

From such small energetic differences between catalysts, the theoretical model presented here was not able to reproduce the observed efficiency trend for these catalysts. In fact, it is probable that the real systems present energy differences which have the same magnitude as the ones obtained here. Although small energy differences may lead to distinguishable experimental efficiency, such small variations are beyond the accuracy of the method employed. The precise reason why high steric demand of the NHC appears to be necessary for high activity could thus not be identified at this point. Nonetheless, valuable mechanistic insights have been obtained (e.g. through pathways that can safely be excluded because of unsurmountable barriers) and the identification of probable rate-limiting steps (in particular the difficult transmetalation step) can form the basis for further rational design of catalysts for this important type of reaction.

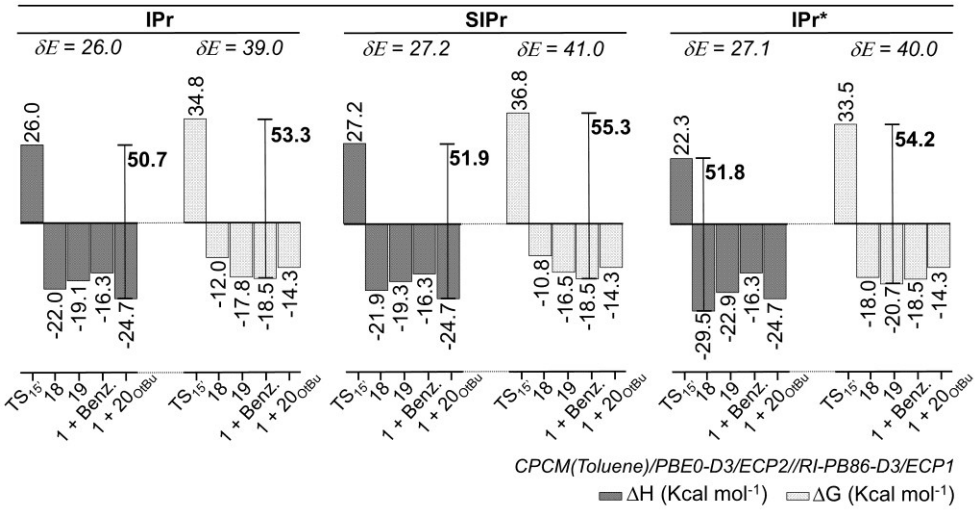

Figure 9. Energy variation (enthalpy and Gibbs free energy, bold) between the rate-determining transiton state **15'$_{NHC}$** and the lower points in the energy profiles, and the calculated energy span (italic) for each ligand. The relative energy of **1** + **20$_{OtBu}$** was considered for calculation of $\Delta E_{Reaction}$.

Conclusions

Four alternative mechanism have been investigated for carboxylation of organoboronates with CO_2 using [Ni(NHC)(Allyl)Cl] complexes (**1$_{NHC}$**, NHC = **IMe**, **IPr**, **SIPr** and **IPr***) as catalysts.

Cycloaddition of CO_2 to the catalysts **1$_{NHC}$** was shown to be kinetically disfavored in the initial steps. Instead, the proposed mechanism starts with the reaction between the catalyst **1$_{NHC}$** (NHC = **IMe**, **IPr**, **SIPr** and **IPr***) and borate. Next, the catalytic cycle proceeds through two pathways, which are connected by the chloride association/elimination equilibrium of the intermediates. The rate-determining step was identified as being the transmetalation process, with computed relative free-energy barriers of 34.8, 36.8 and 33.5 kcal mol^{-1} for **1$_{IPr}$**, **1$_{SIPr}$** and **1$_{IPr*}$**, respectively.

The energy span for the catalytic cycle of **1$_{IPr}$**, **1$_{SIPr}$** and **1$_{IPr*}$** presented values ranging from 26.0 to 27.2 kcal mol^{-1} and from 39.0 to 41.0 kcal mol^{-1} for enthalpy and free-energy, respectively.

Methodology

Optimizations and frequency calculations were carried out for intermediates and transition states at RI-BP86/ECP1 level,[16] in which ECP1 corresponds to the combination of the relativistic SDD pseudopotential[17] for nickel atom and 6-31G* basis-set for the lighter atoms. This level has performed well for molecular structures of metal complexes from the transition metal first row. [18] Each stationary point was confirmed as a minimum or transition structure by computing the number of imaginary frequencies using harmonic approximation.

Single-point energy were calculated for the optimized structures at the PBE0-D3/ECP2 level,[19] in which ECP2 corresponds to the combination of the relativistic SDD pseudopotential for the nickel atom and 6-311+G** basis-set for the lighter atoms, and -D3 denotes two and three-body dispersion correction terms, calculated with the DFT-D3 software [20], including Becke–Johnson damping. [21] Implicit solvation effects were included by the conductor-like polarizable continuum model (CPCM) [22] with the parameters of toluene.

The total enthalpy and Gibbs free energy for each structure were then calculated by the sum of single point energy and thermochemistry corrections obtained at RI-BP86/ECP1 level:

H(PBE0-D3) = E(PBE0-D3) + H(RI-BP86) - E(RI-BP86)
G(PBE0-D3) = E(PBE0-D3) + G(RI-BP86) - E(RI-BP86)

All computations were carried out with the Gaussian09 software package.[23]

Acknowledgements

The authors acknowledge FAPERJ for providing research grants and financial support. MB thanks the School of Chemistry and EaStCHEM for support and for access to a computer cluster maintained by Dr H. Früchtl. JWMC acknowledges CNPq for a research grant. The experimental work was supported via our membership of the UK Catalysis Hub consortium funded by EPSRC (grants EP/K014706/2, EP/K014668/1, EP/K014854/1 and EP/K014714/1). SPN gratefully acknowledges the European Commission for support in the form of an ERC Advanced Researcher grant (227817-FUNCAT)

Keywords: Nickel • N-Heterocyclic carbene • Carbon dioxide • Carboxylation • DFT

References

1. M. Cokoja, C. Bruckmeier, B. Rieger, W. A. Herrmann, F. E. Kühn. *Angew. Chem. Int. Ed. Engl.*, **2011**, *50*, 8510-8537.

2. Y. Tsuji, T. Fujihara, *Chem. Commun*., **2012**, *48*, 9956-9964.
3. Y. Sasaki, Y. Inoue, H. Hashimoto, *J. Chem. Soc. Chem. Commun*., **1976**, 605-606..
4. Y. Inoue, Y. Itoh, H. Hashimoto, *Chem. Lett.* **1977** *6*, 855-856.
5. K. Ukai, M. Aoki, J. Takaya, N. Iwasawa, *J. Am. Chem. Soc.*, **2006**, *128*, 8706-8707.
6. J. Takaya, S. Tadami, K. Ukai, N. Iwasawa, *Org. Lett.* **2008**, *10*, 2697-2700.
7. T. Ohishi, M. Nishiura, Z. Hou, *Angew. Chem. Int. Ed. Engl.*, **2008**, *47*, 5792-5795.
8. X. Zhang, W.-Z. Zhang, L.-L. Shi, C.X. Guo, L.-L. Zhang, X.-B. Lu, *Chem. Comm.*, **2012**, *48*, 6292-6294.
9. Y.Makida, E. Marelli, A. M. Z. Slkawin, S. P. Nolan *Chem. Comm.*, **2014**, *50*, 8010-8013.
10. For selected examples, see: a) C. S. Yeung, V. M. Dong, *J. Am. Chem. Soc.* **2008**, *130*, 7826–7827; b) H. Ochiai, M. Jang, K. Hirano, H. Yorimitsu, K. Oshima, *Org. Lett.* **2008**, 10, 2681–2683; c) L. Zhang, J. Cheng, T. Ohishi, Z. Hou, *Angew. Chem. Int. Ed. Engl.* **2010**, *49*, 8670–8673; d) I. I. F. Boogaerts, G. C. Fortman, M. R. L. Furst, C. S. J. Cazin, S. P. Nolan, *Angew. Chem. Int. Ed. Engl.* **2010**, *49*, 8674–8677; e) I. I. F. Boogaerts, S. P. Nolan, *J. Am. Chem. Soc.* **2010**, *132*, 8858–8859; f) H. Mizuno, J. Takaya, N. Iwasawa, *J. Am. Chem. Soc.* **2011**, *133*, 1251–1253; g) Y. Liu, J. Cornella, R. Martin, *J. Am. Chem. Soc.* **2014**, *136*, 11212–11215; h) A. Correa, T. León, R. Martin, *J. Am. Chem. Soc.* **2014**, *136*, 1062–1069, i) T. León, A. Correa, R. Martin, *J. Am. Chem. Soc.* **2013**, *135*, 1221–1224; j) T. Moragas, J. Cornella, R. Martin, *J. Am. Chem. Soc.* **2014**, *136*, 17702–17705; k) P. Shao, S. Wang, C. Chen, C. Xi, *Org. Lett*. **2016**, *18*, 2050–2053; l) X. Zhang, X. Xie, Y. Liu, *Chem. Sci.* **2016**, *7*, 5815–5820.
11. M. Aresta, C.F. Nobile, V.G. Albano, E. Forni, and M. Manassero,, J. Chem. Soc. *Chem. Comm*, **1975**, 636-637.
12. D. M. Denning, D.E. Falvey, *J. Org. Chem.* **2017**, *82*, 1552-1557.
13. S. Kozuch, S. Shaik,. *J. Am. Chem. Soc.* **2006**, *128*, 3355-3365.
14. a) R. D. J. Froese, in Computational Modeling for Homogeneous and Enzymatic Catalysis, K. Morokuma, D. G. Musaev (Eds.), Wiley-VCH, Weinheim 2008, Chapter 7, pp. 149-179; b) J. Cooper, T. Ziegler, *Inorg. Chem.* **2002**, *41*, 6614-6622.
15. R. L. Martin, P. J. Hay, L. R. Pratt, *J. Phys. Chem. A*, **1998**, *102*, 3565-3573.
16. a) A. D. Becke, *Phys. Rev. A* **1988**, *38*, 3098-3100; b) J. P. Perdew, *Phys. Rev.B*, **1986**, *33*,8822-8824.
17. M. Dolg, H. Stoll, H. Preuss, R. M. Pitzer, *J. Phys. Chem.* **1993**, *97*,5852-5859.
18. M. Buhl, H. Kabrede, *J. Chem. Theory Comput.*, **2006**, *2*, 1282-1290.
19. a) J. P. Perdew, K. Burke, M. Ernzerhof, *Phys.Rev. Lett.* **1996**, *77*,3865–3868; b) J. P. Perdew, K. Burke, M. Ernzerhof, *Phys.Rev. Lett.* **1997**, *78*, 1396..
20. a) S. Grimme, J. Antony, S. Ehrlich, H. Krieg, *J. Chem. Phys*. **2010**, *132*, 154104. b) S. Grimme, S. Ehrlich, L. Goerigk, *J. Comput. Chem.* **2011**, *32*, 1456-1465. c) T. Risthaus, S. Grimme, *J. Chem. Theory Comput.* **2013**, *9*, 1580-1591.
21. a) A. D. Becke, E. R. Johnson, *J. Chem. Phys.* **2005**, *122*, 154104. b) E. R. Johnson, A. D. Becke, *J. Chem. Phys*. **2006**, *124*, 174104.
22. a) Y. Takano, K. Houk, *J. Chem. Theory Comput.* **2005**, *1*, 70-77; b) J. Tomasi, B. Mennucci, R. Cammi, , *Chem. Rev*. **2005**, *105*, 2999-3094.
23. Gaussian 09, Revision D.01, M. J. Frisch, G. W. Trucks, H. B. Schlegel, G. E. Scuseria, M. A. Robb, J. R. Cheeseman, G. Scalmani, V. Barone, B. Mennucci, G. A. Petersson, H. Nakatsuji, M. Caricato, X. Li, H. P. Hratchian, A. F. Izmaylov, J. Bloino, G. Zheng, J. L. Sonnenberg, M. Hada, M. Ehara, K. Toyota, R. Fukuda, J. Hasegawa, M. Ishida, T. Nakajima, Y. Honda, O. Kitao, H. Nakai, T. Vreven, J. A. Montgomery, Jr., J. E. Peralta, F. Ogliaro, M. Bearpark, J. J. Heyd, E. Brothers, K. N. Kudin, V. N. Staroverov, T. Keith, R. Kobayashi, J. Normand, K. Raghavachari, A. Rendell, J. C. Burant, S. S. Iyengar, J. Tomasi, M. Cossi, N. Rega, J. M. Millam, M. Klene, J. E. Knox, J. B. Cross, V. Bakken, C. Adamo, J. Jaramillo, R. Gomperts, R. E. Stratmann, O. Yazyev, A. J. Austin, R. Cammi, C. Pomelli, J. W. Ochterski, R. L. Martin, K. Morokuma, V. G. Zakrzewski, G. A. Voth, P. Salvador, J. J. Dannenberg, S. Dapprich, A. D. Daniels, O. Farkas, J. B. Foresman, J. V. Ortiz, J. Cioslowski, and D. J. Fox, Gaussian, Inc., Wallingford CT, **2013**.

Table of Contents

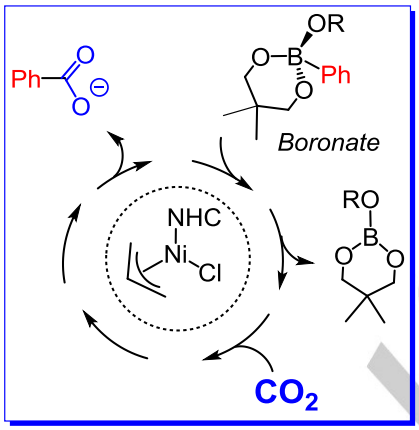

CO_2 Activation. Based on DFT calculations a new mechanism is proposed for the Ni-catalysed carboxylation of organoboronates with CO_2. In this mechanism, transfer of the organic moiety from boron to nickel (transmetalation) is identified as the rate-limiting step.